Adjusting solar-induced fluorescence to nadir-viewing provides a better proxy for GPP

Dalei Hao [a], Yelu Zeng [a,b,*], Zhaoying Zhang [c,d], Yongguang Zhang [c,d], Han Qiu [a,b], Khelvi Biriukova [e], Marco Celesti [e], Micol Rossini [e], Peng Zhu [f], Ghassem R. Asrar [g], Min Chen [a,b,h,*]

[a] *Joint Global Change Research Institute, Pacific Northwest National Laboratory, College Park, MD, USA*
[b] *Department of Forest and Wildlife Ecology, University of Wisconsin-Madison, Madison, WI, USA*
[c] *International Institute for Earth System Sciences, Jiangsu Center for Collaborative Innovation in Geographical Information Resource Development and Application, Nanjing University, Nanjing, Jiangsu, China*
[d] *Jiangsu Provincial Key Laboratory of Geographic Information Science and Technology, Key Laboratory for Land Satellite Remote Sensing Applications of Ministry of Natural Resources, School of Geography and Ocean Science, Nanjing University, Nanjing, Jiangsu, China*
[e] *Remote Sensing of Environmental Dynamics Laboratory, Department of Earth and Environmental Sciences (DISAT), University of Milano-Bicocca, Piazza della Scienza 1, Milano, Italy*
[f] *Laboratoire des Sciences du Climat et de l'Environnement, CEA-CNRS-UVSQ, UMR8212, Gif-sur-Yvette, France*
[g] *Universities Space Research Association, Columbia, MD, USA*
[h] *Nelson Institute Center for Climatic Research, University of Wisconsin-Madison, Madison, WI, USA*

A R T I C L E I N F O

Keywords:
SIF
Gross primary productivity
Viewing-angle effects
Nadir viewing
Canopy structure effects
TROPOMI

A B S T R A C T

Solar-induced fluorescence (*SIF*) provides key information for inferring terrestrial gross primary productivity (*GPP*). However, there is little research on analyzing the performance of nadir-adjusted *SIF* (SIF_{nadir}) on *GPP*, compared to total *SIF* emitted by all leaves (SIF_{total}) for reducing the viewing angle effects and estimating *GPP*. Besides, there have been controversial opinions on whether SIF_{total} is better correlated to *GPP* than raw SIF observations (SIF_{obs}). Here we systematically analyzed the relationship between raw/nadir/total *SIF* (i.e., SIF_{obs}, SIF_{nadir} and SIF_{total}) and *GPP* and investigated the underlying mechanism, using multi-angular field measurements and eddy covariance data in wheat and corn crops at sub-daily scale. We further compared the performance of SIF_{obs}, SIF_{nadir} and SIF_{total} in estimating GPP using the TROPOspheric Monitoring Instrument (TROPOMI) *SIF* and concurrent AmeriFlux measurements at daily scale. The results indicate that diurnal SIF_{nadir} has stronger cor-relations to *GPP* than SIF_{obs} for field measurements, with the increase of mean coefficient of determination (R^2) by 0.05–0.07 for far-red band and 0.11–0.20 for red band. SIF_{nadir} shows comparable performance with SIF_{total} for both far-red and red bands. Although the viewing angle effects dominate the difference in estimating GPP be-tween SIF_{nadir} and SIF_{obs}, the correlation between light use efficiency (*LUE*) and f_{esc} further determines the different performance of SIF_{nadir} and SIF_{total} in estimating GPP. TROPOMI-based analysis further confirms that SIF_{nadir} overall has higher correlations to AmeriFlux *GPP* than SIF_{obs} for different plant functional types and shows similar performance with SIF_{total}. Compared to SIF_{total}, the estimation of SIF_{nadir} independent of viewing angle effects does not require any canopy structure parameters, and thus offers promising potential for reliably estimating regional and global *GPP*.

1. Introduction

The emerging spaceborne solar-induced fluorescence (*SIF*) measurements offer a novel opportunity for monitoring and interpreting large-scale ecosystem carbon cycle (Frankenberg et al., 2011; Joiner et al., 2011; Magney et al., 2020; Meroni et al., 2009; Mohammed et al., 2019; Ryu et al., 2019). Compared to traditional vegetation indices, *SIF* has more inherent linkages to vegetation photosynthetic activities (Gu et al., 2019; Magney et al., 2019). *SIF* has been increasingly used for tracking terrestrial gross primary productivity (*GPP*) (Sun et al., 2017),

* Corresponding authors at: Department of Forest and Wildlife Ecology, University of Wisconsin-Madison, Madison, WI, USA.
E-mail addresses: zeng74@wisc.edu (Y. Zeng), mchen392@wisc.edu (M. Chen).

https://doi.org/10.1016/j.isprsjprs.2022.01.016
Received 30 June 2021; Received in revised form 22 December 2021; Accepted 21 January 2022

detecting plant stress (He et al., 2020b; Song et al., 2018), monitoring vegetation phenology (Wang et al., 2019; Zhang et al., 2020a), estimating crop yield (Guan et al., 2016; He et al., 2020a) and diagnosing ecosystem transpiration (Lu et al., 2018; Maes et al., 2020; Shan et al., 2019; Shan et al., 2021).

However, viewing-angle effects have considerable impact on the top- of-canopy *SIF* observations (SIF_{obs}) and their applications. Similar to surface reflectance, SIF_{obs} is sensitive to viewing angles due to the can-opy scattering and re-absorption processes (Van der Tol et al., 2019), which has been confirmed by field measurements (Biriukova et al., 2020; Liu et al., 2015; Pinto et al., 2017; Rogers et al., 2020; Zhang et al., 2020c), model simulations (Sakai et al., 2020; Zeng et al., 2020; Zhao et al., 2016) and remote sensing observations (Doughty et al., 2019; Guanter et al., 2012). The viewing-angle effects on *SIF* can distort the *SIF-GPP* relationship (Zhang et al., 2019a; Zhang et al., 2018b; Zhang et al., 2021). Considering that most existing and upcoming *SIF* obser-vations from spaceborne instruments such as the Second Global Ozone Monitoring Experiment (GOME-2), Orbiting Carbon Observatory-2 (OCO-2) and TROPOspheric Monitoring Instrument (TROPOMI) have varying scanning angles, reducing the view-angle effects is urgently needed for *SIF* applications.

Compared to SIF_{obs}, the total *SIF* emitted by all leaves (hereinafter referred to as total *SIF, SIF_{total}*) is less affected by scattering and reabsorption processes, and thus has been considered to be better correlated to *GPP* (He et al., 2017; Lu et al., 2020; Zhang et al., 2019b; Zhang et al., 2020b; Zhang et al., 2020c). A few recent studies developed practical methods to estimate SIF_{total} based on radiative transfer modeling (Liu et al., 2019; Yang and Van der Tol, 2018; Yang et al., 2020; Zeng et al., 2019). These methods typically require knowledge of canopy structure parameters such as leaf area index (*LAI*), clumping index (*CI*) and leaf angle distribution (*LAD*), but their estimations from remote sensing still have large uncertainties (Fang et al., 2019; Pisek et al., 2015; Zhang et al., 2020d) and hinder robust applications of SIF_{total}.

Moreover, there have been controversial opinions on whether SIF_{total} is better correlated to *GPP* than SIF_{obs}. Zhang et al. (2019b, 2020b) used the spaceborne TROPOMI and OCO-2 data and demonstrated that SIF_{total} outperformed SIF_{obs} because of the reduced impact of canopy structure effect. Lu et al. (2020) showed SIF_{total} improved the estimate of diurnal *GPP* at Harvard Forest with complex canopy structure. Zhang et al. (2020c) showed that SIF_{total} had less angular dependencies and stronger relationship with GPP in crops. In contrast, Dechant et al. (2020) showed SIF_{obs} better served as a proxy for *GPP* in crops, benefited by the positive correlations of the ratio of *SIF* photons escaping from canopy with photosynthetic light use efficiency (*LUE*). It is worth noting that the viewing angle of *SIF* measurements was fixed at nadir or hemispheric in Dechant et al. (2020), whereas *SIF* observations were collected at varying viewing angles in Zhang et al. (2019b, 2020b, 2020c), and with a fixed view zenith angle (*VZA*) of 30° in Lu et al. (2020). The datasets used in the existing studies were collected using different modes of fixed (nadir or off-nadir) or varying viewing angles, and thus the conclusions of these studies may not be directly comparable and scalable. The viewing-angle effects have smaller impacts on analyzing the *SIF-GPP* relationship in Dechant et al. (2020) due to nadir or hemispherical viewing conditions, as compared with other studies (e.g., Zhang et al. (2019b, 2020b, 2020c) and Lu et al. (2020)) with time varying viewing conditions, which may explain the contradictory conclusions from these studies.

Therefore, normalizing SIF_{obs} to a standard viewing angle (i.e., nadir in this study) is proposed in this study to minimize the viewing-angle effects on SIF_{obs}. This effort will facilitate a systematic analysis on the impacts of viewing angle on the *SIF-GPP* relationship and an evaluation of the capabilities of nadir-adjusted *SIF* (SIF_{nadir}) and SIF_{total} for approximating GPP, which can potentially resolve the aforementioned debate. To the best of our knowledge, no such analysis has been carried out before. Compared to off-nadir viewing angles, SIF_{nadir} is less prone to be affected by hotspot effects caused by the variation of solar angles (Hao et al., 2021a). Liu et al. (2016) explored the potential of kernel-driven (KD) Bidirectional-Reflectance-Distribution-Function (BRDF) models in fitting multi-angular *SIF* measurements. Hao et al. (2021b) developed two practical methods to normalize *SIF* to nadir-viewing: one was based on multi-angular reflectance while the other leveraged a KD model (Hao et al., 2020b). Neither method requires input of canopy structural parameters, and their performance only depends on high- quality reflectance and *SIF* data.

Our study aims to comprehensively assess and understand the performance of SIF_{nadir} and SIF_{total} on approximating *GPP* estimations. We primarily focus on answering the following four questions : 1) how effective are different *SIF* normalization methods in reducing the viewing-angle effects? 2) how does SIF_{obs} normalized to nadir viewing perform in estimating *GPP*, compared to the raw off-nadir SIF_{obs}? 3) which is better for estimating photosynthesis, SIF_{nadir} or SIF_{total}? and 4) what are the contributing factors leading to the differences between the performance of SIF_{nadir} and SIF_{total}?

2. Materials and methods

2.1. Multi-angular field SIF measurements at sub-daily scale

First, two field datasets (wheat and corn crops) were used in our analysis, with the characteristics presented in Table 1. Both wheat and corn canopies show the erectophile leaf inclination distribution (empirically identified from the field). Specifically, a high-resolution spectrometer QEPro (Ocean Optics, Dunedin, FL, USA) installed in a multi-angular measurement system (Multi-Fluo) was used to collect multi-angular observations. It had a field-of-view (FOV) of 25° and a spectral range of 650–800 nm, with a full width at half maximum of 0.3 nm. For each day, the Multi-Fluo system (Fig. S1) collected 24 groups (with different VZAs) of multi-angular data from 6:00 to 18:00 (UTC+8). The system acquired one group of multi-angular observations with the same VZA every 30 min, which covered 25 different view azimuth an-gles (*VAA*) changing from 60° to 300° at a 10° interval. During the measurements, *VZA* was dynamically adjusted to track the solar zenith angle (*SZA*) and to capture the hotspot effects, and it was fixed at 40° when $SZA > 40°$ to avoid the effects of large instantaneous FOVs. An advanced spectral fitting method (Cogliati et al., 2015) was used to retrieve *SIF* for far-red (760 nm) and red (687 nm) wavelengths. We used the averaged reflectance for 686–691 nm and 757–768 nm spectral bandwidths as Red and near-infrared (NIR) reflectance, respectively. During the growing season, an eddy covariance flux system was installed to continuously measure net ecosystem CO_2 exchange (*NEE*). Accom-panying meteorological data composed of shortwave radiation, air temperature, relative humidity and vapor pressure deficit were observed regularly. *GPP* was estimated at a half-hourly interval using a nighttime- based partitioning method (Reichstein et al., 2005) provided in the REddyProc tool (Wutzler et al., 2018). Effective *LAI* (equal to *LAI·CI,* denoted as *eLAI*) was measured with LAI-2200 plant canopy analyzer (LI-COR, Lincoln, NE, USA). The photosynthetically active radiation (*PAR*) and fraction of *PAR* absorbed by chlorophyll (*FPAR*) were measured via six LI-190SL quantum sensors (LI-COR Inc., Lincoln, NE, USA) installed both above and below the canopy, and *LUE* was calcu-lated as *GPP/* (*PAR·FPAR*). We only used the data acquired under clear sky conditions when the clearness index (defined as the ratio of top-of-canopy to top-of-atmosphere solar radiation) was larger than 0.6 to avoid the interference of clouds. Finally, the field data obtained for five days were used in the analysis. Detailed descriptions of the field datasets and associated quality control can be found in Zhang et al. (2020c).

2.2. TROPOMI SIF and MODIS data

We also used daily TROPOMI *SIF* data over 2018–2019 together with corresponding MODIS products and flux tower GPP data from AmeriFlux sites (see Section 2.3) to evaluate our analysis at the large spatial scale.

TROPOMI onboard the Sentinel-5 Precursor provides near-daily (around 13:30) *SIF* data with global coverage and a spatial resolution of 3.5-km × 7-km at nadir (Köhler et al., 2018). Considering that retrieved red *SIF* from TROPOMI still has high relative uncertainties (Köhler et al., 2020), we only used far-red (740 nm) *SIF* in this study. We used both instantaneous and daily averaged *SIF* and calculated the daily averaged *SIF* using the day-length correction factors (Zhang et al., 2018a). To reduce the cloud contamination and keep the most possible valid *SIF* data, the *SIF* soundings with the cloud fraction greater than 0.5 were excluded and the sensitivity of our results to this threshold was tested (see Section 3.3). Considering the large uncertainty in a single TRO-POMI measurement (Köhler et al., 2018), *SIF* measurements centering within a 10-km radius of the flux towers were averaged to reduce the SIF uncertainties (Frankenberg et al., 2014) and match the AmeriFlux *GPP*.

A set of 500-m MODIS data were collected at the selected AmeriFlux sites using the Google Earth Engine (GEE) (Gorelick et al., 2017) to provide vegetation information. Specifically, the IGBP layer in the yearly MCD12Q1-v6 land cover products (Friedl et al., 2002) for 2018 was used to evaluate the homogeneity of AmeriFlux sites. The sites with larger than 50% being covered by the dominant PFT within a 10-km radius of the tower were considered as homogeneous. The 4-day MCD15A3H-v6 *LAI/FPAR* products (Myneni et al., 2002) were selected to provide *LAI* and *FPAR*. The 8-day *CI* data retrieved from MODIS were acquired from Wei et al. (2019). Daily MCD43A1-v6 BRDF/Albedo Model Parameters products (Schaaf et al., 2002) were used to estimate multi-angular reflectance. The MODIS pixels within a 1.5-km radius of the flux towers were spatially-averaged and temporally-interpolated using a nearest neighbor methods to match with the AmeriFlux *GPP*.

2.3. AmeriFlux GPP data

Overall, 102 AmeriFlux sites which have coincident measurements with TROPOMI *SIF* during 2018–2019 were selected for our analysis (see Table S1 and Fig. 1 for site information and spatial distribution, respectively). These sites cover eight International-Geosphere-Biosphere-Programme (IGBP) PFTs (Belward et al., 1999): Evergreen needleleaf forests (ENF), Deciduous broadleaf forests (DBF), Mixed forests (MF), Open shrublands (OSH), Woody savannas (WSA), Grasslands (GRA), Wetlands (WET), and Croplands (CRO). Half-hourly *GPP* data estimated from partitioning NEE measurements at these sites were aggregated to acquire the daily values. Both half-hourly and daily *GPP* data were used to match with the instantaneous and daily averaged TROPOMI *SIF* data, respectively. Only the *GPP* data during the growing seasons from April to October were used to avoid the impact of dormancy in winter.

2.4. Decoupling viewing-angle and scattering/reabsorption effects on SIF

2.4.1. Overall framework

Due to the BRDF effect, SIF_{obs} is impacted by both the solar and viewing angles. With a certain solar angle, SIF_{obs} at a wavelength (λ) and a viewing angle (Ω) can be conceptually modeled as (Lee et al., 2013; Sun et al., 2017):

$$SIF_{obs}(\Omega,\lambda) = PAR \cdot FPAR \cdot \Phi_F(\lambda) \cdot f_{esc}(\Omega,\lambda) \tag{1}$$

where Φ_F is the quantum yield of *SIF*, and f_{esc} represents the fraction of *SIF* photons escaping from canopy. The product of first three terms represents SIF_{total} within a canopy.

We can directly derive SIF_{total} from SIF_{obs} using Equation (1) as:

$$SIF_{total}(\lambda) = \frac{SIF_{obs}(\Omega,\lambda)}{f_{esc}(\Omega,\lambda)} \tag{2}$$

Equation (2) suggests that the effects of viewing-angle and scattering/reabsorption can be simultaneously minimized. However, to

Table 1
Characteristics of the field measurements for wheat and corn crops.

Variables		Wheat	Corn
Location	Latitude (°N)	34.5199	34.5199
	Longitude (°E)	115.5916	115.5916
Measured Time	Year	2018	2018
	Day of Year (DOY)	124–133	235–239
	Hour of day	6:00–18:00	6:00–18:00
Viewing angle	View Zenith Angle (*VZA*, °)	20–40	15–40
	View Azimuth Angle (*VAA*, °)	60–300 at 10 intervals	60–300 at 10 intervals
Leaf parameter	Leaf chlorophyll content (*Cab*, μg cm^{-2})	66–71	51–54
Canopy structure	Effective leaf area index (*eLAI*, m^2 m^{-2})	5.2–5.8	2.8–2.9
	Leaf inclination angle distribution	Erectophile	Erectophile
Field Image			

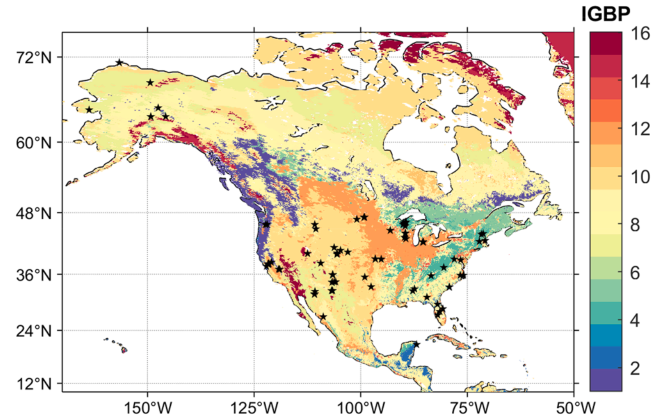

Fig. 1. Spatial distribution of AmeriFlux sites used in our study. Black pentagram represents the site location. The background color represents the IGBP PFTs: 1: Evergreen needleleaf forests, ENF; 2: Evergreen broadleaf forests, EBF; 3: Deciduous needleleaf forests, DNF; 4: Deciduous broadleaf forests, DBF; 5: Mixed forests, MF; 6: Closed shrublands, CSH; 7: Open shrublands, OSH; 8: Wood savannas, WSA; 9: Savannas, SAV; 10: Grasslands, GRA; 11: Permanent wetlands, WET; 12: Croplands, CRO; 13: Urban and built-up lands, URB; 14: Cropland/natural vegetation mosaics: CVM; 15: Snow and ice, SNO; and 16: Barren, BSV.

evaluate their separate effects on SIF_{obs}, we need to decouple them into two independent terms. A practical solution for achieving this objective is to: 1) normalize SIF_{obs} with varying viewing angles to a standard viewing geometry (e.g., nadir) and 2) estimate SIF_{total} from SIF_{nadir}. In the first step, all *SIF* observations are corrected to an identical viewing angle and thus the viewing-angle effects are minimized/eliminated; and in the second step, the scattering/reabsorption effects can be further mini-mized by estimating SIF_{total}.

2.4.2. Calculating f_{esc} for deriving total SIF

Equation (2) shows that the key to disentangling the effects of viewing-angle and scattering/reabsorption is to accurately calculate f_{esc}. Based on the spectral invariants theory, Yang and van der Tol (2018) derived a simple method to calculate far-red f_{esc}:

$$f_{esc}(\Omega, far\_red) = \frac{Ref(\Omega, far\_red)}{i_0 \cdot \omega(far\_red)} \tag{3}$$

where *Ref* represents the NIR reflectance, i_0 is the canopy interceptance which represents the probability of a photon interacting with the vegetation canopy (Smolander and Stenberg, 2005), and ω is the leaf single scattering albedo (equal to the sum of leaf reflectance and transmittance). This method is only suitable for dense vegetation canopy (Yang and van der Tol, 2018). Zhang et al. (2020c) used this equation to empirically estimate red f_{esc}. i_0 can be calculated using canopy structure parameters (Chen and Leblanc, 2001):

$$i_0 = 1 - \exp\left[\frac{-\mathrm{G(SZA)} \cdot \mathrm{LAI} \cdot \mathrm{CI}}{\cos(\mathrm{SZA})}\right] \tag{4}$$

where G(*SZA*) is the leaf projection function which quantifies the projection coefficient of unit foliage area on a plane perpendicular to the illumination direction. This method requires accurate canopy structure parameters (e.g., *LAI*, *CI* and *LAD*).

Meanwhile, Zeng et al. (2019) developed a practical method for estimating far-red f_{esc} using the near-infrared reflectance of vegetation (*NIRv*) (Badgley et al., 2017) and *FPAR*:

$$f_{esc}(\Omega, far\_red) = \frac{NIRv(\Omega)}{FPAR \cdot \omega(far\_red)} \tag{5}$$

$$NIRv \approx NIR \cdot NDVI \tag{6}$$

where *NIRv* represents the fraction of reflected NIR light that originates from vegetation, and *NDVI* is the normalized difference vegetation index (Tucker, 1979). This method requires accurate estimation of *NIRv* and *FPAR*. Compared to Eq. (3), this method is suitable for both dense and sparse vegetation canopies (Zeng et al., 2019).

Similarly, Liu et al. (2020) developed a method for estimating red f_{esc} using the red reflectance of vegetation (*Redv*) and *FPAR*:

$$f_{esc}(\Omega, red) = \frac{Redv(\Omega)}{FPAR \cdot \omega(red)} \tag{7}$$

$$Redv(\Omega) \approx Red \cdot NDVI^2 \tag{8}$$

where *Redv* represents the fraction of reflected red light that originates from vegetation. $NDVI^2$ is used to reduce the contribution of soil to red reflectance, which is only an approximation acquired based on the PROSAIL model (Liu et al., 2020). This method also requires an accurate estimation of *Redv* and *FPAR*.

Hereinafter, we named the methods expressed in Equations (3)–(4) and Equation (5)–(8) as i_0-based and *FPAR*-based methods, respectively. In this study, we also compared the difference between derived SIF_{total} using *Ref* (Equation (3)) and *NIRv* (Equation (6)) or *Redv* (Equation (8)).

2.4.3. Viewing-angle normalization methods

Based on Equation (1), SIF_{nadir} can be calculated by

$$SIF_{nadir}(\lambda) = SIF_{obs}(\Omega, \lambda) \cdot \frac{f_{esc}(nadir, \lambda)}{f_{esc}(\Omega, \lambda)} \tag{9}$$

Combining Equations (5)–(8) and (9), we can normalize SIF_{obs} to SIF_{nadir} only with *NIRv* or *Redv* at both nadir and observed directions, which can be acquired from the KD model. This method is hereafter referred as the *NIRv*/*Redv*-based method. This method is applicable when multi-angular reflectance data are available, but its performance depends on the reduced sensitivty of *NIRv* and *Redv* to soil contribution (Hao et al., 2021b).

Hao et al. (2021b) suggested an alternative method that uses the KD model to fit *PAR*-normalized multi-angular *SIF* observations (hereinafter referred to as KD-based method):

$$\frac{SIF_{obs}(\Omega, \lambda)}{PAR} = f_{iso}(\lambda) \cdot K_{iso}(\Omega) + f_{vol}(\lambda) \cdot K_{vol}(\Omega) + f_{geo}(\lambda) \cdot K_{geo}(\Omega) \tag{10}$$

where f_{iso}, f_{vol} and f_{geo} represent the fitting parameters, and K_{iso}, K_{vol} and K_{geo} represent the isotropic, volumetric-scattering and geometric-optical kernels. In this study, we used a constant value of 1, RossThick kernel and LiTransit kernel as K_{iso}, K_{vol} and K_{geo}, respectively, to capture the BRDF shapes caused by volumetric-scattering and surface-scattering. The RossThick kernel was derived from a single scattering approxima-tion of the radiative transfer theory for dense vegetation canopy (Rou-jean et al., 1992), and the LiTransit kernel was derived from the geometric-optical mutual shadowing BRDF model for sparse vegetation canopy (Li et al., 1999). RossThick kernel and LiTransit kernel can be used to characterize bowl-shaped and dome-shaped BRDF curves, respectively.

Considering relatively small variations of Φ_F within one day (Yang et al., 2018) or during the growing season (Wang et al., 2020) and relatively stable canopy structure in a short time period, we can use multiple *SIF* observations to fit the KD model in Equation (10) and then derive the ratio of SIF_{nadir} to SIF_{obs}. This method is efficient only when multi-angular *SIF* and *PAR* data are available, and its performance also depends on employed KD models (Hao et al., 2021b).

2.5. Analysis and evaluation methods

Using the field dataset at sub-daily scale, we first fitted the KD models to all reflectance and *SIF* observations for each day; then used the fitted models to calculate nadir reflectance and *SIF* at each time of that day. Finally, SIF_{nadir} and SIF_{total} were estimated using the methods in Sections 2.4.2 and 2.4.3. We evaluated the performance of adjusted *SIFs* by four methods (two methods for estimating SIF_{nadir} and two methods for estimating SIF_{total}) for estimating *GPP*. Note that for i_0-based and *FPAR*-based methods, ω were assumed as 0.9 and 0.1 for far-red and red bands, respectively (Liu et al., 2019), assuming that ω has little variation during the short measurement periods (Table 1). i_0 was estimated based on measured *eLAI* and a simplified approximation of $G(SZA) = 0.5$ under the spherical distribution. For the *FPAR*-based method, we used the measured *FPAR*. We assume that the *SIF* variation is caused mainly by the variation of viewing angle in a short time window (i.e., 30 min) under no-stress conditions and thus the coefficient of variation (CV) was used to evaluate the performance of different methods for reducing the viewing-angle effects, calculated as the ratio of standard deviation to mean value:

$$CV = \frac{std(\{SIF_i\})}{mean(\{SIF_i\})} \tag{11}$$

where$\{SIF_i\}$ represents the group of observed/nadir/total *SIF*. Specifically, we calculated the CVs for each group of *SIF* values with the same *VZA* but different *VAAs*, where the raw *SIF* observed data were acquired at a short time window of about 30 min and thus the variation of the solar angle can be neglected. Smaller CVs indicate better performance for reducing the viewing-angle effects.

We used both linear and hyperbolic models (Damm et al., 2015) to approximate the empirical *SIF-GPP* relationship:

$$GPP = a1 \cdot SIF + b1 \tag{12}$$

$$GPP = \frac{a2 \cdot SIF}{SIF + b2} \tag{13}$$

where *SIF* represents observed/nadir/total *SIF*, and $a1$, $a2$, $b1$ and $b2$ are the fitting parameters. We used the coefficient of determination (R^2) and root mean square errors (RMSE) to test the goodness of fit for linear models, and the RMSE for hyperbolic models. The relationship was considered statistically significant if the significance level (p-value) was smaller than 0.05.

We used the TROPOMI and AmeriFlux data (both instantaneous at the overpass time of TROPOMI and daily averaged values) over the 2018–2019 period to evaluate the *SIF-GPP* relationship at the large spatial scale. Table S2 provides an overview of the data source for canopy structure parameters and reflectance, used for different methods. With the KD-based method, TROPOMI SIF data in a 16-day window were used to fit the parameters in the KD model. With the i_0-based method, the far-red ω were assumed to be 0.9 (Asner, 1998; Gates et al., 1965; Liu et al., 2019) and relatively conservative both within and across species and is relatively invariant across time and space. LAD was assumed to be spherical, and then i_0 was estimated using MODIS LAI and CI data. With the *FPAR*-based method, ω was also assumed to be 0.9 and MODIS *FPAR* data was used. The magnitude of far-red ω only affected the magnitude of f_{esc} and had minimal impacts on the results in our study due to its small variations with time.

3. Results

3.1. Minimizing viewing-angle effects on SIF

Both SIF_{nadir} and SIF_{total} reduce the angular heterogeneity of *SIF* observations in wheat and corn, compared to raw directional *SIF* observations (Figs. 2 and 3). Overall, the KD model fits well with the reflectance and *SIF* for wheat and corn (Fig. 2). Nadir *SIF* has smaller CVs than the raw directional *SIF* observations (Fig. 3). For wheat, nadir *SIF* normalized by *NIRv/Redv*-based method has mean CVs of about 14.2% (far-red) and 29.8% (red), and the mean CVs of KD-based method are 17.7% (far-red) and 25.3% (red), while the raw multi-angular observations have mean CVs of 18.7% (far-red) and 44.6% (red). For corn, nadir *SIF* normalized by *NIRv/Redv*-based method has mean CVs of 14.0% (far-red) and 24.7% (red), and the mean CVs of KD-based method are 18.7% (far-red) and 22.8% (red), while observed *SIF* has CV values of 20.5% and 32.8%, respectively. In contrast, the two methods (*FPAR*- based and i_0-based) for calculating total *SIF* have similar mean CVs of 14.2% (far-red) and 29.9% (red) for wheat and 14.2% (far-red) and 24.6% (red) for corn, respectively. Overall, nadir *SIF* performs similarly as total *SIF* in reducing the viewing angle effects. Using TOC reflectance instead of *NIRv/Redv* leads to similar results (Fig. S2). Fig. S2 shows that the relative SIF (calculated as the ratio of raw *SIF* to reflected radiance) also has good performance in reducing the view-angle effects, which is identical to the TROPOMI-based analysis reported by Magney et al. (2019). Fig. 4 shows the time series of half-hourly observed, nadir and

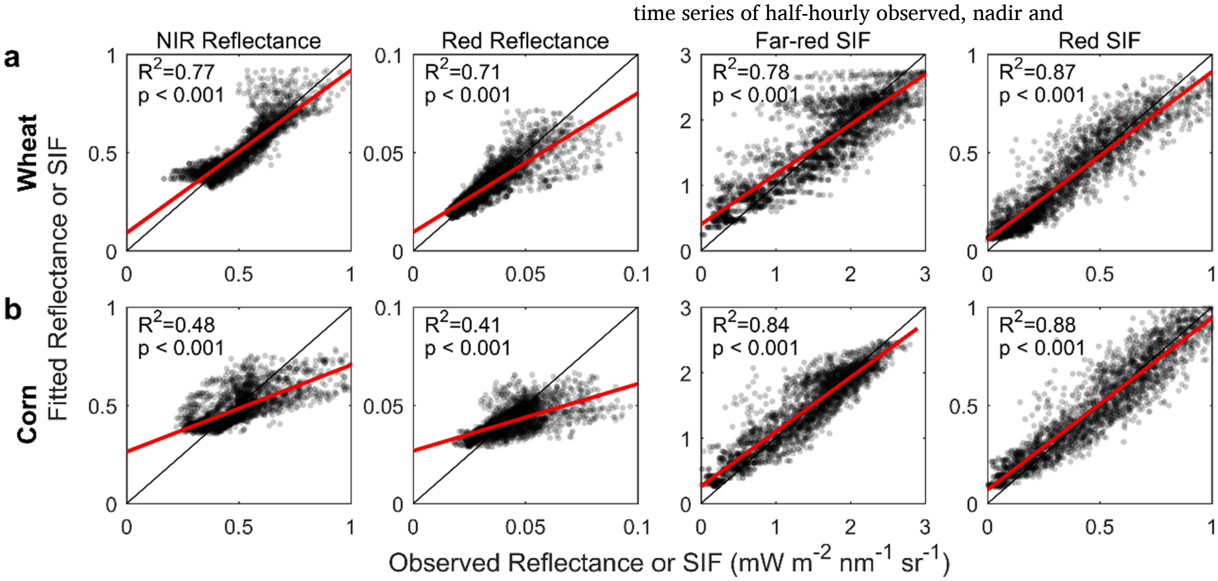

Fig. 2. Comparison between observed and fitted reflectance and *SIF* values with the kernel-driven model for red and far-red bands for **(a)** wheat and **(b)** corn. In each subplot, the degree of transparency for each point represents the data density from low (white) to high (black); the red line represents the linear regression line; and the R^2 and p-values of the linear fitting are also presented. (For interpretation of the references to color in this figure legend, the reader is referred to the web version of this article.)

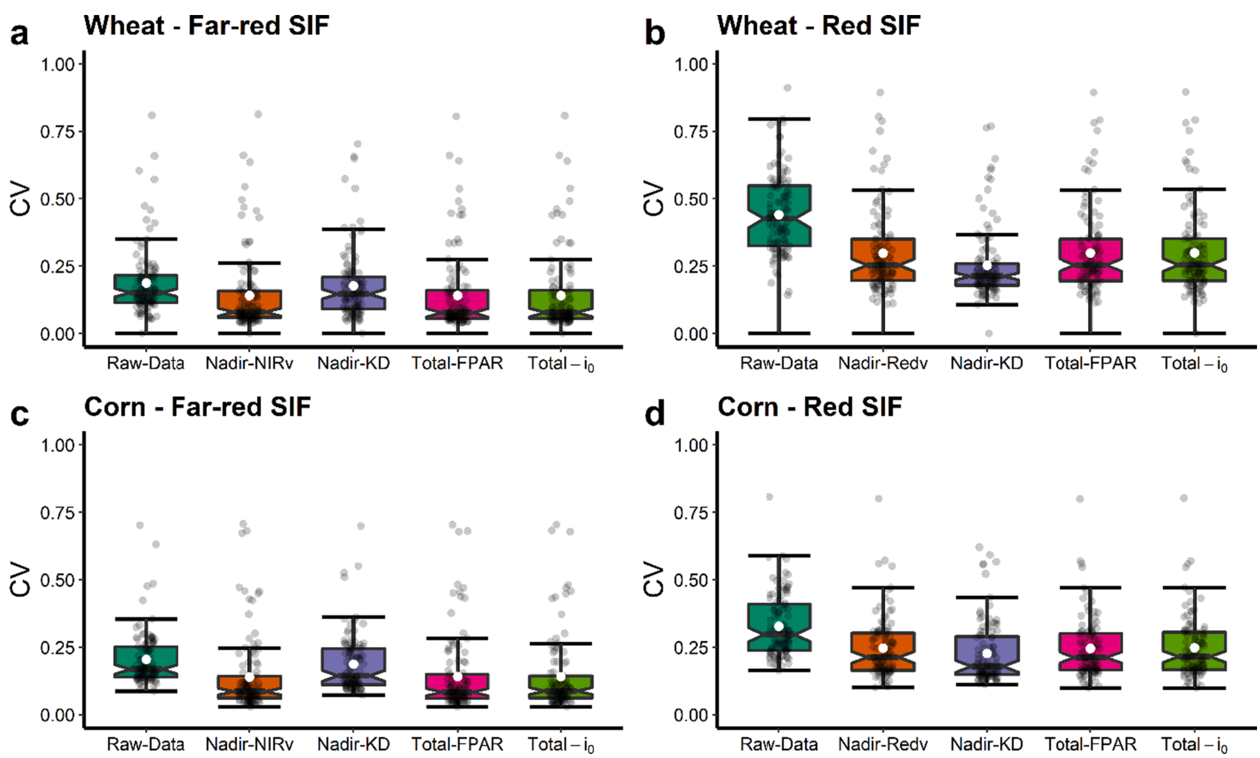

Fig. 3. The coefficient of variation (CV) for observed/nadir/total *SIFs* for far-red and red bands for wheat (a-b) and corn (c-d). Here, CVs were calculated from each group of *SIF* values with the same *VZA* but different *VAAs*, where the raw observed data were acquired at a short time window of about 30 min. 'Raw-data', 'Nadir- NIRv/Redv', 'Nadir-KD', 'Total-FPAR' and 'Total-i_0' represent the raw observed *SIF*, nadir *SIFs* normalized by *NIRv/Redv*- and the KD-based methods, and total *SIFs* calculated by *FPAR*- or i_0-based methods, respectively. For each boxplot, white circles represent the mean values; the central lines represent the median values; boxes represent the interquartile ranges of the 25th (Q_{25}) and 75th (Q_{75}) percentiles; whiskers represent the values of Q_{25}-1.5·(Q_{75}-Q_{25}) and Q_{75} + 1.5·(Q_{75}-Q_{25}); and grey points represent all CV values, whose degree of transparency represents the data density from low (white) to high (black). (For interpretation of the references to color in this figure legend, the reader is referred to the web version of this article.)

total *SIFs*, and the shaded areas of both nadir and total SIFs representing the standard deviations of *SIFs* are generally narrower than raw observed SIF. This further demonstrates that both nadir and total SIFs reduce the viewing-angle effects, when compared to raw *SIF* observations.

3.2. SIF-GPP relationship based on multi-angular field measurements at sub-daily scale

SIF_{nadir} is better correlated to *GPP* than observed multi-angular SIF_{obs} (Fig. 5), due to the reduced viewing-angle effects (Section 3.1). For the linear relationship, when the *VAA* is fixed to be 240° and varying *VZA* (as a case), SIF_{obs} has R^2 values of 0.68 (far-red) and 0.35 (red) in wheat, and 0.59 (far-red) and 0.36 (red) in corn, respectively, while SIF_{nadir} normalized by the *NIRv/Redv*-based method has R^2 values of 0.78 (far- red) and 0.60 (red) in wheat and 0.68 (far-red) and 0.66 (red) in corn; and SIF_{nadir} normalized by the KD-based method has R^2 values of 0.77 (far-red) and 0.68 (red) in wheat and 0.74 (far-red) and 0.78 (red) in corn (see Fig. 5). For all cases of *VAA* in Fig. 6, SIF_{obs} has mean R^2 values of 0.66 (far-red) and 0.37 (red) in wheat and 0.60 (far-red) and 0.53 (red) in corn; the *NIRv/Redv*-based method has mean R^2 values of 0.73 (far-red) and 0.52 (red) in wheat and 0.64 (far-red) and 0.64 (red) in corn; and the KD-based method has mean R^2 values of 0.70 (far-red) and 0.58 (red) in wheat and 0.65 (far-red) and 0.63 (red) in corn. The im-provements (i.e., the increases of R^2 value, ΔR^2) of SIF_{nadir} estimated by the two viewing angle normalization methods can reach up to 0.27 (far- red) and 0.31 (red) in wheat, and 0.18 (far-red) and 0.28 (red) in corn (see Fig. S3). Specifically, for wheat, the ΔR^2 values for the KD-based method vary from − 0.01 to 0.10 for far-red band with an average value of 0.04, and from 0.02 to 0.49 with an average value of 0.20 for red band; and the ΔR^2 values for corn vary from − 0.09 to 0.35 for far-red band with an average value of 0.10 and from − 0.06 to 0.17 for red band with an average value of 0.05 (Fig. S3). The hyperbolic model generally has smaller RMSEs than linear model, especially for the red band in wheat, but SIF_{nadir} has smaller RMSEs than SIF_{obs} for the two models (Fig. 5 and S4-S5).

SIF_{nadir} shows comparable performance for estimating *GPP* to SIF_{total}. The *FPAR*-based and i_0-based methods of calculating SIF_{total} achieve very similar results. Here we only report the results of SIF_{total} calculated based on *FPAR*. For the linear relationship, when *VAA* is 240°, SIF_{total} has R^2 values of 0.76 (far-red) and 0.63 (red) in wheat, and 0.69 (far-red) and 0.66 (red) in corn, which are similar to SIF_{nadir} results (Fig. 5). For all cases of *VAA* shown in Fig. 6, the mean R^2 values are 0.69 (far-red) and 0.59 (red) in wheat, and 0.64 (far-red) and 0.63 (red); and the ΔR^2 values for SIF_{total} are similar to those for SIF_{nadir} (Fig. 3). For RMSE, SIF_{nadir} and SIF_{total} still hold the similar results for linear and hyperbolic models (see Fig. 6 and S4-S5).

3.3. f_{esc} explains the different performance of SIF_{total} and SIF_{nadir}

As shown in Equation (2), the SIF photon escape ratio in the viewing angle, f_{esc}, represents the differences between SIF_{nadir} and SIF_{total}. Thus the relative performance of SIF_{nadir} and SIF_{total} on approximating *GPP* depends on how well f_{esc} is correlated with *LUE*. Fig. 7 shows that nadir f_{esc} at the far-red wavelength has a strong positive correlation to *LUE*, which is consistent with results reported by Dechant et al. (2020). This explains why SIF_{nadir} is slightly better than SIF_{total} in Figs. 5-6. However, the red f_{esc} is weakly or even negatively correlated with *LUE*, resulting that SIF_{nadir} is slightly inferior compared to SIF_{total} (Figs. 5-6). It is worth noting that Equations (7)–(8) are empirical approximations and large uncertainties remain in calculating red f_{esc} (Liu et al., 2020) due to the large differences between leaf reflectance and transmittance in red band

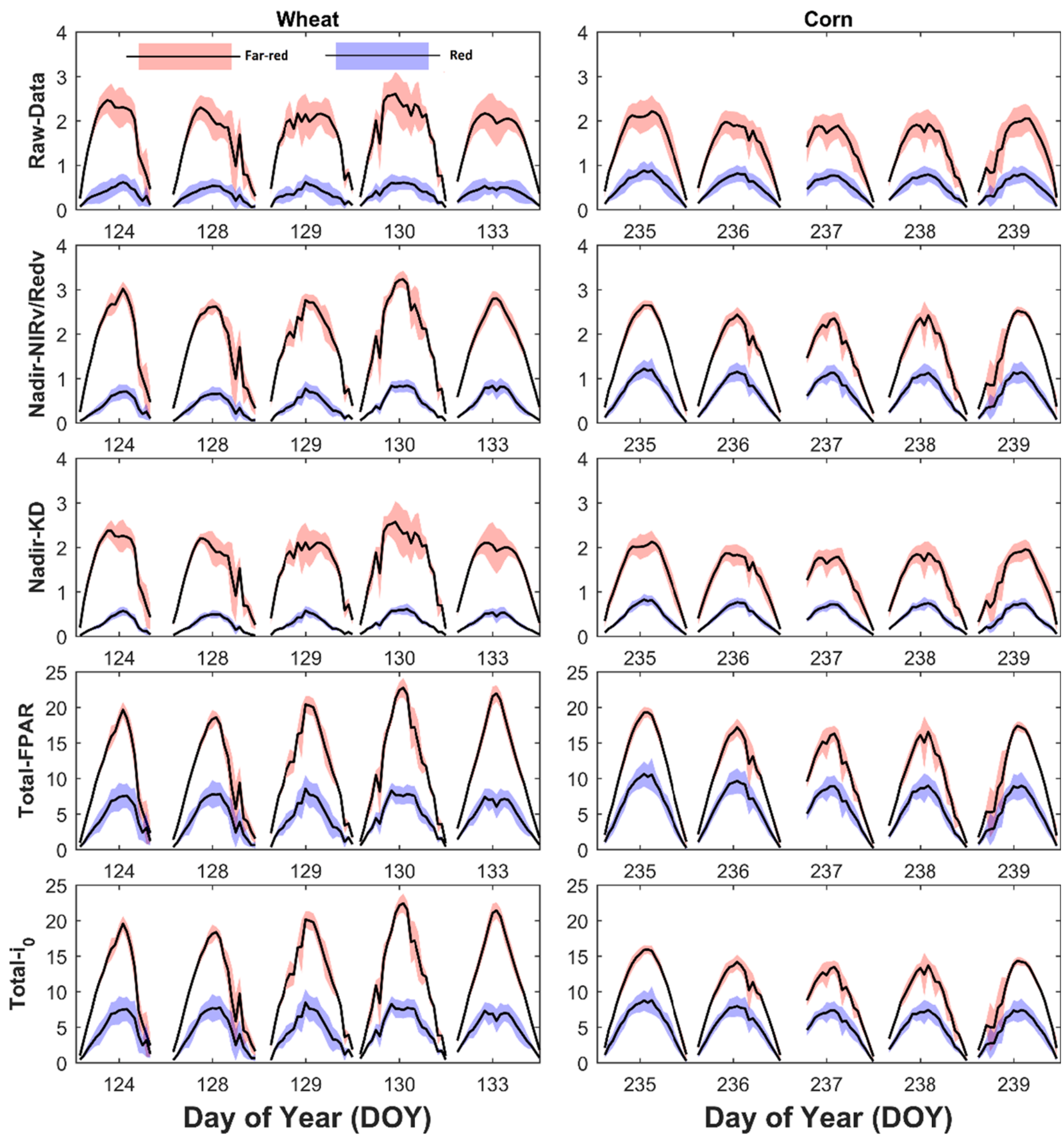

Fig. 4. Time series of half-hourly raw observed, nadir and total SIFs (mW m^{-2} nm^{-1} (sr^{-1})) from 6:00–17:30 (UTC+8) in 2018, for wheat and corn. The black lines and shaded areas represent the mean and standard deviations of *SIF* values, every 30 min.

(Van der Tol et al., 2019; Yang et al., 2020).

3.4. Applications to daily TROPOMI data

Overall, the TROPOMI far-red SIF_{nadir} has higher correlations to AmeriFlux *GPP* than SIF_{obs} and shows similar performance with SIF_{total} for different PFTs, except MF and OSH (Fig. 8). Both SIF_{nadir} and SIF_{total} improved instantaneous *SIF-GPP* relationship at most of the study sites, and the improvement of R^2 and RMSE (i.e., ΔR^2 and ΔRMSE) can exceed 0.1 and 1 μmol·m^{-2}·s^{-1} at several sites for ENF and CRO. Specifically, with the *KD*-based method, the ΔR^2 values of all ENF sites vary from − 0.13 to 0.21 and its average value is 0.05; and the ΔR^2 values for CRO vary from − 0.01 to 0.11 with an average value of 0.05. However, after correcting to SIF_{nadir} and SIF_{total}, the *SIF-GPP* relationship becomes weaker at a few sites. For example, for the *KD*-based method, the ΔR^2 values of all GRA sites vary from − 0.18 to 0.10 and its average value is 0.02. With the daily values, the improvements in R^2 and RMSE can exceed 0.2 and 1 gC·m^{-2}·day^{-1} at several CRO sites. Specifically, with the *KD*-based method, the ΔR^2 values at ENF sites vary from − 0.16 to 0.24 with an average value of 0.06; and the ΔR^2 values at CRO sites vary from − 0.01 to 0.18 with an average value of 0.06; and at GRA sites they vary from − 0.19 to 0.18 and with average value of 0.02. Different viewing angle normalization methods generally show similar perfor-mance, but *NIRv/Redv*-based method performs the best for MF; the KD- based method performs the best for ENF and CRO; and *FPAR*-based and i_0-based methods has better performance for sparse vegetation canopies (i.e., OSH, WSA and GRA). Overall, the results from our analyses of using only homogeneous sites (Fig. S6) are similar to those using all study sites (Fig. 8). In addition, Fig. 8 and S7-S8 show that using different cloud fractions thresholds (i.e., 0.2, 0.5 and 0.8) has minimal impact on the results.

4. Discussion

SIF_{nadir} shows better performance than raw multi-angular *SIF* observations and it has comparable performance as SIF_{total} in estimating *GPP* at both sub-daily and daily scales. Compared to SIF_{obs} with varying viewing angles, both SIF_{nadir} and SIF_{total} effectively reduce the viewing-angle effects (Section 3.1). This explains why SIF_{total} shows better correlations to *GPP* as reported by Zhang et al. (2019b, 2020b, 2020c). Furthermore, even if we adjusted the raw observations to a fixed off-nadir viewing angle (e.g., $VZA = 40^{\circ}$) following Lu et al. (2020), both

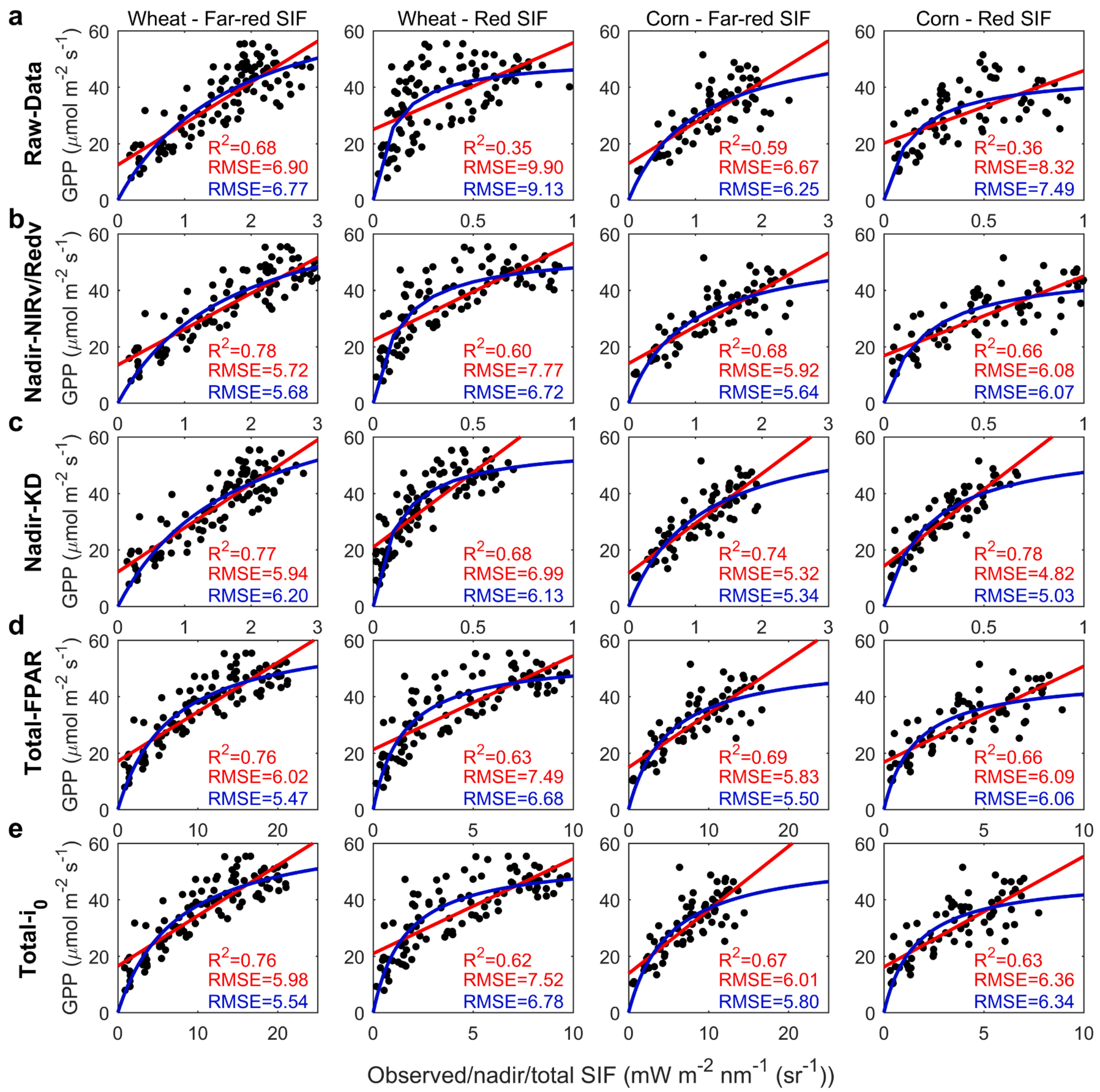

Fig. 5. Performance of observed/nadir/total *SIF*s for far-red and red bands in predicting *GPP* under the *VAA* of 240° but varying *VZA*s for wheat and corn. In each subplot, the red and blue lines represent the linear and hyperbolic fitting lines, respectively; and R^2 and RMSEs of linear fitting are marked by red colors, and RMSEs of hyperbolic fitting are marked by blue colors; p-values are not included because they are smaller than 0.05 in all cases. (For interpretation of the references to color in this figure legend, the reader is referred to the web version of this article.)

SIF_{nadir} and SIF_{total} are still better correlated to *GPP* (Fig. S9). This is likely because SIF_{obs} for an off-nadir angle can be subject to hotspot effects due to solar angle changes, while both SIF_{nadir} and SIF_{total} are less affected by hotspot effects. However, *SIF*s for different viewing angles can convey extra useful information about vegetation canopies. Off- nadir *SIF* measurements may work better at the beginning of the growing season, during which off-nadir sensors receive less soil back-ground (Li et al., 2020). How to make full use of these complementary multi-angular *SIF* data to improve the *GPP* estimations deserves further investigations. It is worth noting that the KD-based method requires high-quality multi-angular *SIF* data but not f_{esc}, and shows better per-formance in red band than the *NIRv/Redv*-based method (Figs. 3 and 5). However, the performance of the KD model is sensitive to the errors and uncertainties of the input *SIF* data (Fig. 2), which likely account for its relatively worse performance in far-red band for wheat (Fig. 6), indi-cating the necessity of reducing the uncertainties of *SIF* retrievals (Chang et al., 2020). The assumptions of constant vegetation structure and Φ_F stands in most cases with sufficient SIF measurements in a short time period, but attentions should be called when the period is long enough or at particular vegetation growing stages, e.g., the early growing season when the plants change rapidly. This method also depends on the choice of kernels in the KD model (Hao et al., 2021b), whose performance needs to be evaluated comprehensively before application.

In concept, SIF_{total} further reduces the scattering/reabsorption effects in addition to the viewing-angle effects, but the correlation between *LUE* and f_{esc} is the key to determine the different performance of SIF_{nadir} and SIF_{total} in approximating GPP (Dechant et al., 2020; Fig. 7). This finding explains the divergent conclusions and debates on the whether SIF_{total} or SIF_{obs} better approximates GPP in previous studies. However, estimating SIF_{total} requires accurate information about canopy structure parame-ters, while normalizing SIF_{obs} to nadir viewing can be achieved using only reflectance or *SIF* data. Recently, a series of global-scale *PAR*, *FPAR*, *LAI* and *CI* datasets have been produced (Hao et al., 2019; Hao et al., 2020a; He et al., 2012; Myneni et al., 2002; Wei et al., 2019), while their uncertainties are widely recognized but usually not well quantified (Fang et al., 2019; Pisek et al., 2015; Zhang et al., 2020d). There is no global *LAD* dataset available yet and a simplified assumption of

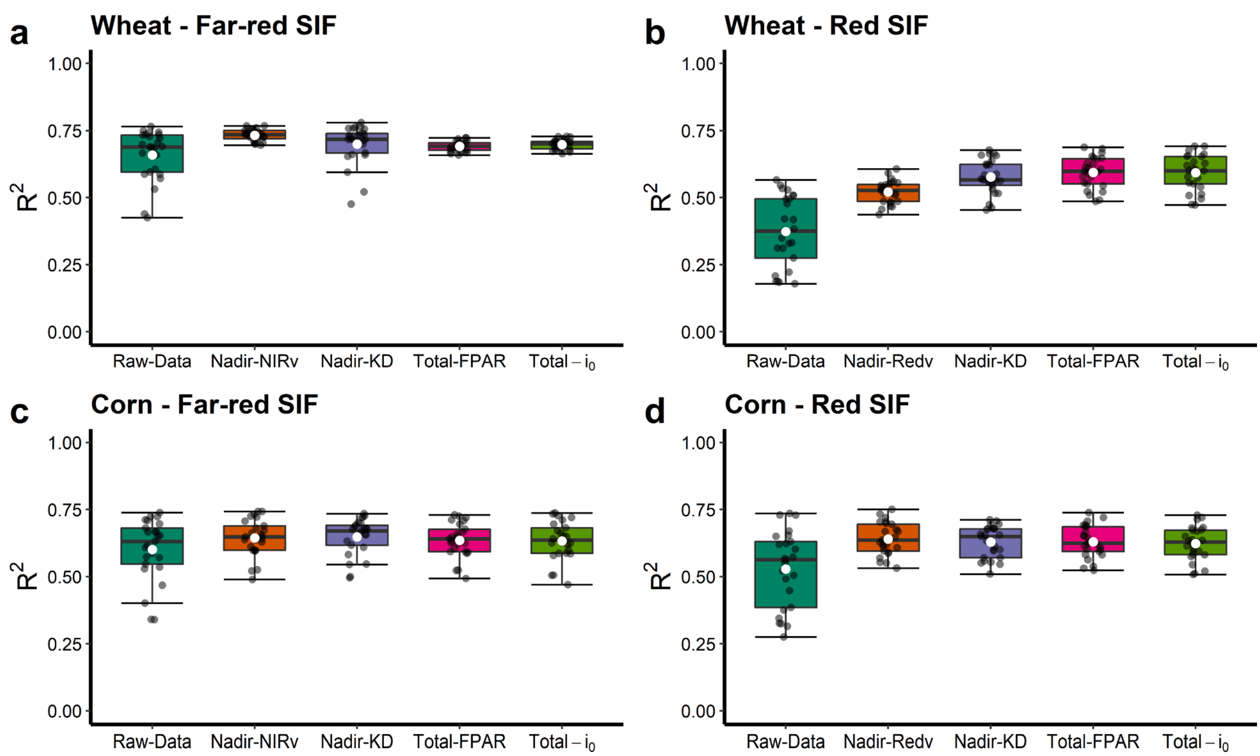

Fig. 6. The R^2 values for the linear relationships between observed/nadir/total *SIFs* for far-red and red bands and *GPP* under different *VAAs* for wheat (a-b) and corn (c-d). For each boxplot, white circles represent the mean values and grey points represent R^2 values. (For interpretation of the references to color in this figure legend, the reader is referred to the web version of this article.)

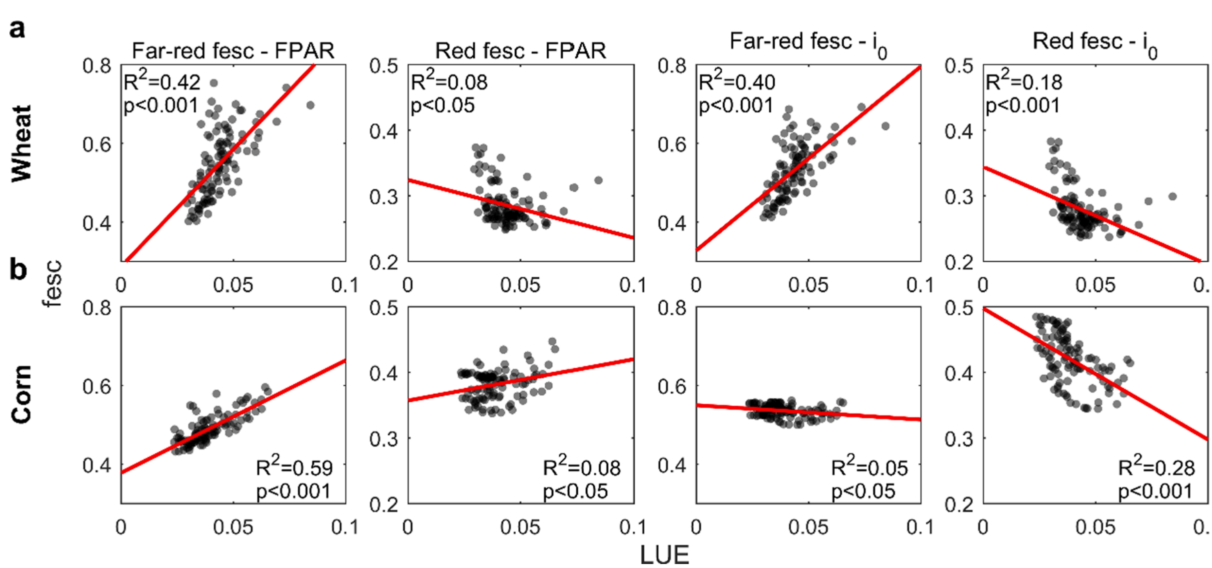

Fig. 7. The relationships between *LUE* and nadir f_{esc} at the far-red and red wavelengths for (a) wheat and (b) corn. Here, 'f_{esc}-FPAR' and 'f_{esc}-i_0' represent the derived *fesc* values by *FPAR*- and i_0 -based methods. In each subplot, the degree of transparency of each point represents the data density from low (white) to high (black); the red line represents the linear regression line; and both R^2 values and *p*-values of linear relationships are also presented. (For interpretation of the references to color in this figure legend, the reader is referred to the web version of this article.)

spherical distribution or prescribed biome-specific *LADs* can introduce additional uncertainties. Accounting for the spatio-temporal variations of ω especially for red band and the effects of diffuse skylight are necessary for estimating SIF_{total} in global applications (Lu et al., 2020).

The relative *SIF* (the ratio of *SIF* to reflected radiance) also has good performance in reducing the view-angle effects (Fig. S2; Magney et al., 2019). However, because the relative *SIF* is calculated as the ratio of *SIF* to reflected radiance, it has a different unit from *SIF* and does not contain the *PAR* information. In fact, the relative *SIF* is proportional to Φ_F (Zeng et al., 2019), which is promising for capturing the physiological response of vegetation to abiotic changes and stresses.

Although overall performance of different methods to angular-normalizing TROPOMI *SIF* data were similar (Fig. 8), small differences can be found due to divergent assumptions of the model/method as well as the quality and accuracy of remote sensing data. Compared to the two methods for estimating SIF_{total}, the two methods for estimating SIF_{nadir}

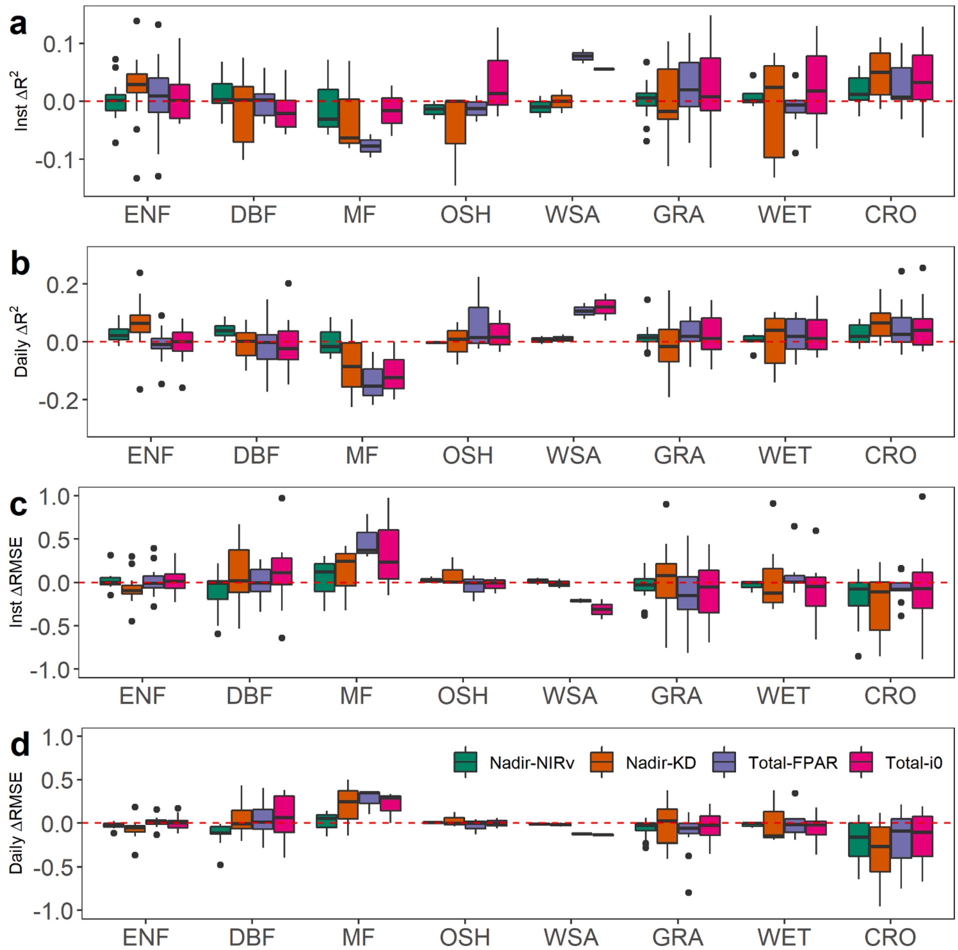

Fig. 8. Changes in goodness of fit (ΔR^2 and ΔRMSE) for the linear fitting between TROPOMI far-red *SIF* and AmeriFlux *GPP* after normalizing observed *SIFs* to nadir or total *SIFs* for all sites with different PFTs. The units of ΔRMSE for instantaneous and daily scales are $\mu mol \cdot m^{-2} \cdot s^{-1}$ and $gC \cdot m^{-2} \cdot day^{-1}$, respectively. (For inter-pretation of the references to color in this figure legend, the reader is referred to the web version of this article.)

do not rely on any inputs of canopy structure parameters and thus they should be more rubust across PFTs. The *NIRv*-based method was derived from Equations (5)–(6), and thus its performance relies on how well *NIRv* can approximate the true NIR reflectance of vegetation (Zeng et al., 2021). Zeng et al. (2021) developed a simple framework for estimating the true *NIRv* from hyperspectral data (NIRvH) with minimized soil contamination, which could be a promising approach for further improving the performance of this method for sparse vegetation can-opies. In theory, the KD-based method is suitable for any PFT if the high- quality *SIF* data is available. However, this method shows poor perfor-mance over OSH, WSA and GRA (Fig. 8), possibly due to the large relative errors of *SIF* retrievals for sparse vegetation canopies. For the methods of estimating SIF_{total}, in principle, the *FPAR*-based method can be applied for both dense and sparse vegetation canopies, while the i_0- based method is primarily suitable for dense canopies. For example, *FPAR*-based method performs the best over WSA for the instantaneous *SIFs*. The fact that these two methods show overall similar performance in our study is possibly due to the uncertainties of canopy structure parameters. Compared to the i_0-based method, the *FPAR*-based method only requires the input of *FPAR*, which is easier to acquire but its ac-curacy require further improvement (Zhang et al., 2020d). Overall, the *SIF* data quality and canopy structure parameters play important roles and may limit their applications in the performance for different PFTs, although the field measurement-based analysis shows that these methods work well for nearly all cases for wheat and corn canopies in this study (Fig. 6 and S3).

We also used both linear and hyperbolic models to test the *SIF-GPP* relationship with and without viewing angle normalizations. The hy-perbolic model generally has higher R^2 values than the linear model (Fig. 5), because LUE can be expressed more realistically as a hyperbolic function of absorbed *PAR* (Damm et al., 2015). This emphasizes the importance of underlying assumptions associated with the model used when evaluating the *SIF-GPP* relationship.

Our results highlight the necessity and feasibility of viewing angle normalization when estimating *GPP* using remotely sensed *SIF*. The two methods for estimating SIF_{nadir} are applicable to TROPOMI data, and SIF_{nadir} from TROPOMI shows a stronger relationship with AmeriFlux *GPP* for most PFTs as compared with SIF_{obs}. These results are not sen-sitive to the cloud cover (Fig. 7 and S6-S7), confirming the robustness of the methods. In addition, most of the existing remote sensing *SIF* data have a varying or off-nadir viewing angle. For example, GOME-2 has a *VZA* of up to 54°; both OCO-2 and OCO-3 (Taylor et al., 2020) have large viewing angles at glint and target modes; and the Geostationary Carbon Observatory (GeoCarb) (Moore et al., 2018) will have large off-nadir viewing angles over the high-latitude regions. To better estimate *GPP*, the viewing-angle effects of *SIF* observations need to be minimized first. Normalizing *SIF* observations to nadir viewing provides a promising way which can avoid the effects of the uncertainties of vegetation canopy parameters. Although simply averaging *SIF* observations over space and time can reduce the viewing angle effects, our study shows the feasibility of viewing angle normalized nadir *SIF* with high spatio-temporal reso-lutions without a need for any space-time smoothing. However, the footprints of TROPOMI can be large if the *SIF* observations are from the edge of the swath, which may not be representative for the dominant

PFT of an eddy covariance tower site. Our results confirm that, our methods can generally work well for both heterogeneous and homogenous study sites (Fig. 7 and S6). The spatial mismatch issues between TROPOMI, MODIS, and AmeriFlux data, spatial heterogeneities and the representativeness of eddy-flux footprints for the tower sites (Chu et al., 2021), may explain the degraded performance of normalized *SIF* for some PFTs (Fig. 8). This issue merits further investigations.

There are still a few limitations in our study. The field datasets we used only cover a short period of a few days of observations and for homogeneous canopies. Using field measurements for the entire growing season, or multiple seasons, over sparse canopies are needed to further evaluate robustness of our proposed methodology. The multi- angular measurements in the study were acquired by dynamically rotating the optical probe, which means the target footprint under different viewing angles was different. The measurements did not cover the full principal (PP) and cross-principal (CPP) planes and thus cannot capture completely the BRDF shapes in PP and CPP. The spectrometer used to obtain the field measurements had a large FOV of 25°, which may lead to uncertainties in the measured multi-angular data. Although TROPOMI data provide unprecedented temporal resolutions, satellite- based *SIF* retrievals are still noisy and have high relative uncertainties for red band (Köhler et al., 2020). Further improving the quality of satellite-based *SIF* retrievals are required for detailed quantitative analysis and applications. In addition, TROPOMI *SIF* data still have sparse spatial resolution, which are hopefully resolved by future mis-sions, such as GeoCarb and the forthcoming Fluorescence Explorer (FLEX) mission of the European Space Agency (Kraft et al., 2017).

5. Conclusions

Directional effects of *SIF* measurements greatly hinder the robust estimation of *GPP*. In this study, we used two practical methods to normalize *SIF* observations to nadir viewing, and used two simple methods to calculate the total *SIF*. We used the multi-angular field measurements for wheat and corn at sub-daily scale, TROPOMI *SIF* and AmeriFlux *GPP* data at daily scale to evaluate their relationships with *GPP*. Our results show that, overall, the four methods show good performance in reducing the viewing angle effects on *SIF*. Nadir *SIF* can better track *GPP* than raw multi-angular observations, due to the reduced viewing angle effects. Nadir *SIF* also shows comparable performance with total *SIF*, but estimating nadir *SIF* only requires reflectance or *SIF* observations, rather than detailed canopy structure parameters generally needed for estimated total *SIF*. The varying relationship of *LUE* and f_{esc} can account for the relative performance of nadir and total *SIF*s on approximating *GPP*. Our results underline the signifi-cance, effectiveness and feasibility of using normalized nadir *SIF* to better estimate *GPP,* especially over large areas.

Declaration of Competing Interest

The authors declare that they have no known competing financial interests or personal relationships that could have appeared to influence the work reported in this paper.

Acknowledgments

This research was supported a Laboratory Directed Research and Development project sponsored by the Pacific Northwest National Laboratory (PNNL) of the U.S. Department of Energy to Min Chen. PNNL is operated by Battelle for the U.S. Department of Energy under Contract DE-AC05-76RL01830. Zhaoying Zhang and Yongguang Zhang were supported by the National Natural Science Foundation of China (42071388) and the fellowship of China Postdoctoral Science Founda-tion (2021M691491). Khelvi Biriukova, Marco Celesti, and Micol Ros-sini were supported by the European Union's Horizon 2020 research and innovation programme under the Marie Skłodowska-Curie grant agreement No. 721995. Marco Celesti was supported by a Living Planet Fellowship (ESA/Contract No. 4000125442/18/I-NS) of the European Space Agency. Multi-angular field data is available through https://doi. org/10.6084/m9.figshare.13011470.v2. We thank Mirco Migliavacca for his contribution to the viewing angle-normalization methods. We acknowledge the AmeriFlux community for sharing the flux data (available at https://ameriflux.lbl.gov/). We also acknowledge Philipp Köhler and Christian Frankenberg for providing useful suggestions and TROPOMI SIF data (available at ftp:// fluo.gps.caltech.edu/data /tropomi/). All MODIS data are available from GEE. Codes to repro-duce all results are available at https:// github.com/daleihao/SIFNorm alization.

Appendix A. Supplementary material

Supplementary data to this article can be found online at https:// doi. org/10.1016/j.isprsjprs.2022.01.016.

References

Asner, G.P., 1998. Biophysical and Biochemical Sources of Variability in Canopy Reflectance. Remote Sens. Environ. 64 (3), 234–253.
Badgley, G., Field, C.B., Berry, J.A., 2017. Canopy near-infrared reflectance and terrestrial photosynthesis. Sci. Adv. 3 (3) https://doi.org/10.1126/sciadv.1602244.
Belward, A.S., Estes, J.E., Kline, K.D., 1999. The IGBP-DIS global 1-km land-cover data set DISCover: A project overview. Photogramm. Eng. Remote Sens. 65, 1013–1020.
Biriukova, K., Celesti, M., Evdokimov, A., Pacheco-Labrador, J., Julitta, T., Migliavacca, M., Giardino, C., Miglietta, F., Colombo, R., Panigada, C., Rossini, M., 2020. Effects of varying solar-view geometry and canopy structure on solar-induced chlorophyll fluorescence and PRI. International Journal of Applied Earth Observation Geoinformation 89, 102069. https://doi.org/10.1016/j. jag.2020.102069.
Chang, C.Y., Guanter, L., Frankenberg, C., Köhler, P., Gu, L., Magney, T.S., Grossmann, K., Sun, Y., 2020. Systematic Assessment of Retrieval Methods for Canopy Far-Red Solar-Induced Chlorophyll Fluorescence Using High-Frequency Automated Field Spectroscopy. Journal of Geophysical Research. Biogeosciences 125 e2019JG005533.
Chen, J.M., Leblanc, S.G., 2001. Multiple-scattering scheme useful for geometric optical modeling. IEEE Transactions on Geoscience Remote Sensing 39 (5), 1061–1071.
Chu, H., Luo, X., Ouyang, Z., Chan, W.S., Dengel, S., Biraud, S.C., Torn, M.S., Metzger, S., Kumar, J., Arain, M.A., Arkebauer, T.J., Baldocchi, D., Bernacchi, C., Billesbach, D., Black, T.A., Blanken, P.D., Bohrer, G., Bracho, R., Brown, S., Brunsell, N.A., Chen, J., Chen, X., Clark, K., Desai, A.R., Duman, T., Durden, D., Fares, S., Forbrich, I., Gamon, J.A., Gough, C.M., Griffis, T., Helbig, M., Hollinger, D., Humphreys, E., Ikawa, H., Iwata, H., Ju, Y., Knowles, J.F., Knox, S.H., Kobayashi, H., Kolb, T., Law, B., Lee, X., Litvak, M., Liu, H., Munger, J.W., Noormets, A., Novick, K., Oberbauer, S.F., Oechel, W., Oikawa, P., Papuga, S.A., Pendall, E., Prajapati, P., Prueger, J., Quinton, W.L., Richardson, A.D., Russell, E.S., Scott, R.L., Starr, G., Staebler, R., Stoy, P.C., Stuart-Haëntjens, E., Sonnentag, O., Sullivan, R.C., Suyker, A., Ueyama, M., Vargas, R., Wood, J.D., Zona, D., 2021. Representativeness of Eddy-Covariance flux footprints for areas surrounding AmeriFlux sites. Agric. For. Meteorol. 301-302, 108350.
Cogliati, S., Verhoef, W., Kraft, S., Sabater, N., Alonso, L., Vicent, J., Moreno, J., Drusch, M., Colombo, R., 2015. Retrieval of sun-induced fluorescence using advanced spectral fitting methods. Remote Sens. Environ. 169, 344–357.
Damm, A., Guanter, L., Paul-Limoges, E., van der Tol, C., Hueni, A., Buchmann, N., Eugster, W., Ammann, C., Schaepman, M.E., 2015. Far-red sun-induced chlorophyll fluorescence shows ecosystem-specific relationships to gross primary production: An assessment based on observational and modeling approaches. Remote Sens. Environ. 166, 91–105.
Dechant, B., Ryu, Y., Badgley, G., Zeng, Y., Berry, J.A., Zhang, Y., Goulas, Y., Li, Z., Zhang, Q., Kang, M., 2020. Canopy structure explains the relationship between photosynthesis and sun-induced chlorophyll fluorescence in crops. Remote Sens. Environ. 241.
Doughty, R., Köhler, P., Frankenberg, C., Magney, T.S., Xiao, X., Qin, Y., Wu, X., Moore, B., 2019. TROPOMI reveals dry-season increase of solar-induced chlorophyll fluorescence in the Amazon forest. Proc. Natl. Acad. Sci. 116 (44), 22393–22398.
Fang, H., Baret, F., Plummer, S., Schaepman-Strub, G., 2019. An overview of global leaf area index (LAI): Methods, products, validation, and applications. Rev. Geophys. 57 (3), 739–799.
Frankenberg, C., Fisher, J.B., Worden, J., Badgley, G., Saatchi, S.S., Lee, J.-E., Toon, G.C., Butz, A., Jung, M., Kuze, A., Yokota, T., 2011. New global observations of the terrestrial carbon cycle from GOSAT: Patterns of plant fluorescence with gross primary productivity. Geophys. Res. Lett. 38 (17).
Frankenberg, C., O'Dell, C., Berry, J., Guanter, L., Joiner, J., Köhler, P., Pollock, R., Taylor, T.E., 2014. Prospects for chlorophyll fluorescence remote sensing from the Orbiting Carbon Observatory-2. Remote Sens. Environ. 147, 1–12.
Friedl, M.A., McIver, D.K., Hodges, J.C.F., Zhang, X.Y., Muchoney, D., Strahler, A.H., Woodcock, C.E., Gopal, S., Schneider, A., Cooper, A., Baccini, A., Gao, F., Schaaf, C.,

2002. Global land cover mapping from MODIS: algorithms and early results. Remote Sens. Environ. 83 (1-2), 287–302.

Gates, D.M., Keegan, H.J., Schleter, J.C., Weidner, V.R., 1965. Spectral Properties of Plants. Appl. Opt. 4 (1), 11. https://doi.org/10.1364/AO.4.000011.

Gorelick, N., Hancher, M., Dixon, M., Ilyushchenko, S., Thau, D., Moore, R., 2017. Google Earth Engine: Planetary-scale geospatial analysis for everyone. Remote Sens. Environ. 202, 18–27.

Gu, L., Han, J., Wood, J.D., Chang, C.-Y., Sun, Y., 2019. Sun-induced Chl fluorescence and its importance for biophysical modeling of photosynthesis based on light reactions. New Phytol. 223 (3), 1179–1191.

Guan, K., Berry, J.A., Zhang, Y., Joiner, J., Guanter, L., Badgley, G., Lobell, D.B., 2016. Improving the monitoring of crop productivity using spaceborne solar-induced fluorescence. Glob. Change Biol. 22 (2), 716–726.

Guanter, L., Frankenberg, C., Dudhia, A., Lewis, P.E., Gómez-Dans, J., Kuze, A., Suto, H., Grainger, R.G., 2012. Retrieval and global assessment of terrestrial chlorophyll fluorescence from GOSAT space measurements. Remote Sens. Environ. 121, 236–251.

Hao, D., Asrar, G.R., Zeng, Y., Yang, X.i., Li, X., Xiao, J., Guan, K., Wen, J., Xiao, Q., Berry, J.A., Chen, M., 2021a. Potential of hotspot solar-induced chlorophyll fluorescence for better tracking terrestrial photosynthesis. Glob. Change Biol. 27 (10), 2144–2158.

Hao, D., Asrar, G.R., Zeng, Y., Zhu, Q., Wen, J., Xiao, Q., Chen, M., 2019. Estimating hourly land surface downward shortwave and photosynthetically active radiation from DSCOVR/EPIC observations. Remote Sens. Environ. 232, 111320. https://doi.org/10.1016/j.rse.2019.111320.

Hao, D., Asrar, G.R., Zeng, Y., Zhu, Q., Wen, J., Xiao, Q., Chen, M., 2020a. DSCOVR/EPIC-derived global hourly and daily downward shortwave and photosynthetically active radiation data at $0.1^\circ \times 0.1^\circ$ resolution. Earth Syst. Sci. Data 12 (3), 2209–2221.

Hao, D., Wen, J., Xiao, Q., You, D., Tang, Y., 2020b. An Improved Topography-Coupled Kernel-Driven Model for Land Surface Anisotropic Reflectance. IEEE Trans. Geosci. Remote Sens. 58 (4), 2833–2847.

Hao, D., Zeng, Y., Qiu, H., Biriukova, K., Celesti, M., Migliavacca, M., Rossini, M., Asrar, G.R., Chen, M., 2021b. Practical approaches for normalizing directional solar-induced fluorescence to a standard viewing geometry. Remote Sens. Environ. 255, 112171. https://doi.org/10.1016/j.rse.2020.112171.

He, L., Chen, J.M., Liu, J., Mo, G., Joiner, J., 2017. Angular normalization of GOME-2 Sun-induced chlorophyll fluorescence observation as a better proxy of vegetation productivity. Geophys. Res. Lett. 44 (11), 5691–5699.

He, L., Chen, J.M., Pisek, J., Schaaf, C.B., Strahler, A.H., 2012. Global clumping index map derived from the MODIS BRDF product. Remote Sens. Environ. 119, 118–130. He, L., Magney, T., Dutta, D., Yin, Y., Köhler, P., Grossmann, K., Stutz, J., Dold, C., Hatfield, J., Guan, K., Peng, B., Frankenberg, C., 2020a. From the Ground to Space: Using Solar-Induced Chlorophyll Fluorescence to Estimate Crop Productivity. Geophys. Res. Lett. 47 e2020GL087474.

He, L., Wood, J.D., Sun, Y., Magney, T., Dutta, D., Köhler, P., Zhang, Y., Yin, Y., Frankenberg, C., 2020b. Tracking seasonal and interannual variability in photosynthetic downregulation in response to water stress at a temperate deciduous forest. Journal of Geophysical Research. Biogeosciences 125 e2018JG005002.

Joiner, J., Yoshida, Y., Vasilkov, A.P., Yoshida, Y., Corp, L.A., Middleton, E.M., 2011. First observations of global and seasonal terrestrial chlorophyll fluorescence from space. Biogeosciences 8 (3), 637–651.

Köhler, P., Behrenfeld, M.J., Landgraf, J., Joiner, J., Magney, T.S., Frankenberg, C., 2020. Global Retrievals of Solar-Induced Chlorophyll Fluorescence at Red Wavelengths With TROPOMI. Geophys. Res. Lett. 47 e2020GL087541.

Köhler, P., Frankenberg, C., Magney, T.S., Guanter, L., Joiner, J., Landgraf, J., 2018. Global Retrievals of Solar-Induced Chlorophyll Fluorescence With TROPOMI: First Results and Intersensor Comparison to OCO-2. Geophys. Res. Lett. 45 (19), 10456–10463.

Kraft, S., Del Bello, U., Harnisch, B., Bouvet, M., Drusch, M., Bézy, J.-L., 2017. Fluorescence imaging spectrometer concepts for the earth explorer mission candidate flex, International Conference on Space Optics—ICSO 2012. International Society for Optics and Photonics, p. 105641W.

Lee, J.-E., Frankenberg, C., van der Tol, C., Berry, J.A., Guanter, L., Boyce, C.K., Fisher, J. B., Morrow, E., Worden, J.R., Asefi, S., 2013. Forest productivity and water stress in Amazonia: Observations from GOSAT chlorophyll fluorescence. Proc. Roy. Soc. B Biol. Sci. 280, 20130171.

Li, D., Chen, J.M., Zhang, X., Yan, Y., Zhu, J., Zheng, H., Zhou, K., Yao, X., Tian, Y., Zhu, Y., Cheng, T., Cao, W., 2020. Improved estimation of leaf chlorophyll content of row crops from canopy reflectance spectra through minimizing canopy structural effects and optimizing off-noon observation time. Remote Sens. Environ. 248, 111985. https://doi.org/10.1016/j.rse.2020.111985.

Li, X., Gao, F., Chen, L., Strahler, A.H., 1999. Derivation and validation of a new kernel for kernel-driven BRDF models, Remote Sensing for Earth Science, Ocean, and Sea Ice Applications. Int. Soc. Opt. Photonics 368–379.

Liu, L., Liu, X., Wang, Z., Zhang, B., 2016. Measurement and analysis of bidirectional SIF emissions in wheat canopies. IEEE Trans. Geosci. Remote Sens. 54 (5), 2640–2651.

Liu, X., Guanter, L., Liu, L., Damm, A., Malenovský, Z., Rascher, U., Peng, D., Du, S., Gastellu-Etchegorry, J.-P., 2019. Downscaling of solar-induced chlorophyll fluorescence from canopy level to photosystem level using a random forest model. Remote Sens. Environ. 231, 110772. https://doi.org/10.1016/j.rse.2018.05.035.

Liu, X., Liu, L., Hu, J., Guo, J., Du, S., 2020. Improving the potential of red SIF for estimating GPP by downscaling from the canopy level to the photosystem level. Agric. For. Meteorol. 281, 107846. https://doi.org/10.1016/j.agrformet.2019.107846.

Lu, X., Liu, Z., An, S., Miralles, D.G., Maes, W., Liu, Y., Tang, J., 2018. Potential of solar-induced chlorophyll fluorescence to estimate transpiration in a temperate forest. Agric. For. Meteorol. 252, 75–87.

Lu, X., Liu, Z., Zhao, F., Tang, J., 2020. Comparison of total emitted solar-induced chlorophyll fluorescence (SIF) and top-of-canopy (TOC) SIF in estimating photosynthesis. Remote Sens. Environ. 251, 112083. https://doi.org/10.1016/j.rse.2020.112083.

Maes, W.H., Pagán, B.R., Martens, B., Gentine, P., Guanter, L., Steppe, K., Verhoest, N.E. C., Dorigo, W., Li, X., Xiao, J., Miralles, D.G., 2020. Sun-induced fluorescence closely linked to ecosystem transpiration as evidenced by satellite data and radiative transfer models. Remote Sens. Environ. 249, 112030. https://doi.org/10.1016/j. rse.2020.112030.

Magney, T.S., Barnes, M.L., Yang, X., 2020. On the Covariation of Chlorophyll Fluorescence and Photosynthesis Across Scales. Geophys. Res. Lett. 47 e2020GL091098.

Magney, T.S., Bowling, D.R., Logan, B.A., Grossmann, K., Stutz, J., Blanken, P.D., Burns, S.P., Cheng, R., Garcia, M.A., Köhler, P., Lopez, S., Parazoo, N.C., Raczka, B., Schimel, D., Frankenberg, C., 2019. Mechanistic evidence for tracking the seasonality of photosynthesis with solar-induced fluorescence. Proc. Natl. Acad. Sci. 116, 11640.

Meroni, M., Rossini, M., Guanter, L., Alonso, L., Rascher, U., Colombo, R., Moreno, J., 2009. Remote sensing of solar-induced chlorophyll fluorescence: Review of methods and applications. Remote Sens. Environ. 113 (10), 2037–2051.

Mohammed, G.H., Colombo, R., Middleton, E.M., Rascher, U., van der Tol, C., Nedbal, L., Goulas, Y., Pérez-Priego, O., Damm, A., Meroni, M., 2019. Remote sensing of solar-induced chlorophyll fluorescence (SIF) in vegetation: 50 years of progress. Remote Sens. Environ. 231, 111177.

Moore III, B., Crowell, S.M.R., Rayner, P.J., Kumer, J., O'Dell, C.W., O'Brien, D., Utembe, S., Polonsky, I., Schimel, D., Lemen, J., 2018. The potential of the geostationary Carbon Cycle Observatory (GeoCarb) to provide multi-scale constraints on the carbon cycle in the Americas. Front. Environ. Sci. 6, 109.

Myneni, R.B., Hoffman, S., Knyazikhin, Y., Privette, J.L., Glassy, J., Tian, Y., Wang, Y., Song, X., Zhang, Y., Smith, G.R., Lotsch, A., Friedl, M., Morisette, J.T., Votava, P., Nemani, R.R., Running, S.W., 2002. Global products of vegetation leaf area and fraction absorbed PAR from year one of MODIS data. Remote Sens. Environ. 83 (1-2), 214–231.

Pinto, F., Müller-Linow, M., Schickling, A., Cendrero-Mateo, M., Ballvora, A., Rascher, U., 2017. Multiangular observation of canopy sun-induced chlorophyll fluorescence by combining imaging spectroscopy and stereoscopy. Remote Sens. 9 (5), 415. https://doi.org/10.3390/rs9050415.

Pisek, J., Govind, A., Arndt, S.K., Hocking, D., Wardlaw, T.J., Fang, H., Matteucci, G., Longdoz, B., 2015. Intercomparison of clumping index estimates from POLDER, MODIS, and MISR satellite data over reference sites. ISPRS J. Photogram. Remote Sens. 101, 47–56.

Reichstein, M., Falge, E., Baldocchi, D., Papale, D., Aubinet, M., Berbigier, P., Bernhofer, C., Buchmann, N., Gilmanov, T., Granier, A., Grunwald, T., Havrankova, K., Ilvesniemi, H., Janous, D., Knohl, A., Laurila, T., Lohila, A., Loustau, D., Matteucci, G., Meyers, T., Miglietta, F., Ourcival, J.-M., Pumpanen, J., Rambal, S., Rotenberg, E., Sanz, M., Tenhunen, J., Seufert, G., Vaccari, F., Vesala, T., Yakir, D., Valentini, R., 2005. On the separation of net ecosystem exchange into assimilation and ecosystem respiration: review and improved algorithm. Glob. Change Biol. 11 (9), 1424–1439.

Rogers, C.A., Chen, J.M., Zheng, T., Croft, H., Gonsamo, A., Luo, X., Staebler, R.M., 2020. The Response of Spectral Vegetation Indices and Solar-Induced Fluorescence to Changes in Illumination Intensity and Geometry in the Days Surrounding the 2017 North American Solar Eclipse. Journal of Geophysical Research. Biogeosciences 125 e2020JG005774.

Roujean, J.-L., Leroy, M., Deschamps, P.-Y., 1992. A bidirectional reflectance model of the Earth's surface for the correction of remote sensing data. J. Geophys. Res. Atmos. 97 (D18), 20455. https://doi.org/10.1029/92JD01411.

Ryu, Y., Berry, J.A., Baldocchi, D.D., 2019. What is global photosynthesis? History, uncertainties and opportunities. Remote Sens. Environ. 223, 95–114.

Sakai, Y., Kobayashi, H., Kato, T., 2020. FLiES-SIF version 1.0: three-dimensional radiative transfer model for estimating solar induced fluorescence. Geosci. Model Dev. 13 (9), 4041–4066.

Schaaf, C.B., Gao, F., Strahler, A.H., Lucht, W., Li, X., Tsang, T., Strugnell, N.C., Zhang, X., Jin, Y., Muller, J.-P., Lewis, P., Barnsley, M., Hobson, P., Disney, M., Roberts, G., Dunderdale, M., Doll, C., d'Entremont, R.P., Hu, B., Liang, S., Privette, J. L., Roy, D., 2002. First operational BRDF, albedo nadir reflectance products from MODIS. Remote Sens. Environ. 83 (1-2), 135–148.

Shan, N., Ju, W., Migliavacca, M., Martini, D., Guanter, L., Chen, J., Goulas, Y., Zhang, Y., 2019. Modeling canopy conductance and transpiration from solar-induced chlorophyll fluorescence. Agric. For. Meteorol. 268, 189–201.

Shan, N., Zhang, Y., Chen, J.M., Ju, W., Migliavacca, M., Peñuelas, J., Yang, X.i., Zhang, Z., Nelson, J.A., Goulas, Y., 2021. A model for estimating transpiration from remotely sensed solar-induced chlorophyll fluorescence. Remote Sens. Environ. 252, 112134. https://doi.org/10.1016/j.rse.2020.112134.

Song, L., Guanter, L., Guan, K., You, L., Huete, A., Ju, W., Zhang, Y., 2018. Satellite sun-induced chlorophyll fluorescence detects early response of winter wheat to heat stress in the Indian Indo-Gangetic Plains. Glob. Change Biol. 24 (9), 4023–4037.

Smolander, S., Stenberg, P., 2005. Simple parameterizations of the radiation budget of uniform broadleaved and coniferous canopies. Remote Sens. Environ. 94 (3), 355–363.

Sun, Y., Frankenberg, C., Wood, J.D., Schimel, D.S., Jung, M., Guanter, L., Drewry, D.T., Verma, M., Porcar-Castell, A., Griffis, T.J., Gu, L., Magney, T.S., Köhler, P., Evans, B., Yuen, K., 2017. OCO-2 advances photosynthesis observation from space via solar-

induced chlorophyll fluorescence. Science 358 (6360). https://doi.org/10.1126/science:aam5747.
Taylor, T.E., Eldering, A., Merrelli, A., Kiel, M., Somkuti, P., Cheng, C., Rosenberg, R., Fisher, B., Crisp, D., Basilio, R., Bennett, M., Cervantes, D., Chang, A., Dang, L., Frankenberg, C., Haemmerle, V.R., Keller, G.R., Kurosu, T., Laughner, J.L., Lee, R., Marchetti, Y., Nelson, R.R., O'Dell, C.W., Osterman, G., Pavlick, R., Roehl, C., Schneider, R., Spiers, G., To, C., Wells, C., Wennberg, P.O., Yelamanchili, A., Yu, S., 2020. OCO-3 early mission operations and initial (vEarly) XCO2 and SIF retrievals. Remote Sens. Environ. 251, 112032. https://doi.org/10.1016/j.rse.2020.112032.
Tucker, C.J., 1979. Red and photographic infrared linear combinations for monitoring vegetation. Remote Sens. Environ. 8 (2), 127–150.
van der Tol, C., Vilfan, N., Dauwe, D., Cendrero-Mateo, M.P., Yang, P., 2019. The scattering and re-absorption of red and near-infrared chlorophyll fluorescence in the models Fluspect and SCOPE. Remote Sens. Environ. 232, 111292. https://doi.org/ 10.1016/j.rse.2019.111292.
Wang, C., Beringer, J., Hutley, L.B., Cleverly, J., Li, J., Liu, Q., Sun, Y., 2019. Phenology Dynamics of Dryland Ecosystems Along the North Australian Tropical Transect Revealed by Satellite Solar-Induced Chlorophyll Fluorescence. Geophys. Res. Lett. 46 (10), 5294–5302.
Wang, C., Guan, K., Peng, B., Chen, M., Jiang, C., Zeng, Y., Wu, G., Wang, S., Wu, J., Yang, X.i., Frankenberg, C., Köhler, P., Berry, J., Bernacchi, C., Zhu, K., Alden, C., Miao, G., 2020. Satellite footprint data from OCO-2 and TROPOMI reveal significant spatio-temporal and inter-vegetation type variabilities of solar-induced fluorescence yield in the U.S. Midwest. Remote Sens. Environ. 241, 111728. https://doi.org/ 10.1016/j.rse.2020.111728.
Wei, S., Fang, H., Schaaf, C.B., He, L., Chen, J.M., 2019. Global 500 m clumping index product derived from MODIS BRDF data (2001–2017). Remote Sens. Environ. 232, 111296.
Wutzler, T., Lucas-Moffat, A., Migliavacca, M., Knauer, J., Sickel, K., Šigut, L., Menzer, O., Reichstein, M., 2018. Basic and extensible post-processing of eddy covariance flux data with REddyProc. Biogeosciences 15 (16), 5015–5030.
Yang, K., Ryu, Y., Dechant, B., Berry, J.A., Hwang, Y., Jiang, C., Kang, M., Kim, J., Kimm, H., Kornfeld, A., Yang, X.i., 2018. Sun-induced chlorophyll fluorescence is more strongly related to absorbed light than to photosynthesis at half-hourly resolution in a rice paddy. Remote Sens. Environ. 216, 658–673.
Yang, P., van der Tol, C., 2018. Linking canopy scattering of far-red sun-induced chlorophyll fluorescence with reflectance. Remote Sens. Environ. 209, 456–467.
Yang, P., van der Tol, C., Campbell, P.K.E., Middleton, E.M., 2020. Fluorescence Correction Vegetation Index (FCVI): A physically based reflectance index to separate physiological and non-physiological information in far-red sun-induced chlorophyll fluorescence. Remote Sens. Environ. 240, 111676. https://doi.org/10.1016/j. rse.2020.111676.
Zeng, Y., Badgley, G., Chen, M., Li, J., Anderegg, L.D.L., Kornfeld, A., Liu, Q., Xu, B., Yang, B., Yan, K., Berry, J.A., 2020. A radiative transfer model for solar induced fluorescence using spectral invariants theory. Remote Sens. Environ. 240, 111678. https://doi.org/10.1016/j.rse.2020.111678.
Zeng, Y., Badgley, G., Dechant, B., Ryu, Y., Chen, M., Berry, J.A., 2019. A practical approach for estimating the escape ratio of near-infrared solar-induced chlorophyll fluorescence. Remote Sens. Environ. 232, 111209. https://doi.org/10.1016/j.rse.2019.05.028.
Zeng, Y., Hao, D., Badgley, G., Damm, A., Rascher, U., Ryu, Y., Johnson, J., Krieger, V., Wu, S., Qiu, H., Liu, Y., Berry, J.A., Chen, M., 2021. Estimating near-infrared reflectance of vegetation from hyperspectral data. Remote Sens. Environ. 267, 112723. https://doi.org/10.1016/j.rse.2021.112723.
Zhang, Q., Zhang, Y., Li, Z., Li, J., Zhang, X., 2019a. The effects of sun-viewer geometry on sun-induced fluorescence and its relationship with gross primary production. In: IEEE, pp. 9048–9051.
Zhang, Q., Chen, J.M., Ju, W., Zhang, Y., Li, Z., He, L., Pacheco-Labrador, J., Li, J., Qiu, B., Zhang, X., Qiu, F., Chen, B., Chou, S., Zhang, Z., Shan, N., 2021. Ground-Based Multiangle Solar-Induced Chlorophyll Fluorescence Observation and Angular Normalization for Assessing Crop Productivity. Journal of Geophysical Research. Biogeosciences 126 e2020JG006082.
Zhang, Y., Commane, R., Zhou, S., Williams, A.P., Gentine, P., 2020a. Light limitation regulates the response of autumn terrestrial carbon uptake to warming. Nat. Clim. Change 10 (8), 739–743.
Zhang, Y., Xiao, X., Zhang, Y., Wolf, S., Zhou, S., Joiner, J., Guanter, L., Verma, M., Sun, Y., Yang, X.i., Paul-Limoges, E., Gough, C.M., Wohlfahrt, G., Gioli, B., van der Tol, C., Yann, N., Lund, M., de Grandcourt, A., 2018a. On the relationship between sub-daily instantaneous and daily total gross primary production: Implications for interpreting satellite-based SIF retrievals. Remote Sens. Environ. 205, 276–289.
Zhang, Z., Chen, J.M., Guanter, L., He, L., Zhang, Y., 2019b. From canopy-leaving to total canopy far-red fluorescence emission for remote sensing of photosynthesis: First results from TROPOMI. Geophys. Res. Lett. 46 (21), 12030–12040.
Zhang, Z., Zhang, Y., Joiner, J., Migliavacca, M., 2018b. Angle matters: Bidirectional effects impact the slope of relationship between gross primary productivity and sun-induced chlorophyll fluorescence from Orbiting Carbon Observatory-2 across biomes. Glob. Change Biol. 24 (11), 5017–5020.
Zhang, Z., Zhang, Y., Porcar-Castell, A., Joiner, J., Guanter, L., Yang, X.i., Migliavacca, M., Ju, W., Sun, Z., Chen, S., Martini, D., Zhang, Q., Li, Z., Cleverly, J., Wang, H., Goulas, Y., 2020b. Reduction of structural impacts and distinction of photosynthetic pathways in a global estimation of GPP from space-borne solar-induced chlorophyll fluorescence. Remote Sens. Environ. 240, 111722. https://doi.org/10.1016/j.rse.2020.111722.
Zhang, Z., Zhang, Y., Zhang, Q., Chen, J.M., Porcar-Castell, A., Guanter, L., Wu, Y., Zhang, X., Wang, H., Ding, D., Li, Z., 2020c. Assessing bi-directional effects on the diurnal cycle of measured solar-induced chlorophyll fluorescence in crop canopies. Agric. For. Meteorol. 295, 108147. https://doi.org/10.1016/j.agrformet.2020.108147.
Zhang, Z., Zhang, Y., Zhang, Y., Gobron, N., Frankenberg, C., Wang, S., Li, Z., 2020d. The potential of satellite FPAR product for GPP estimation: An indirect evaluation using solar-induced chlorophyll fluorescence. Remote Sens. Environ. 240, 111686. https:// doi.org/10.1016/j.rse.2020.111686.
Zhao, F., Dai, X.u., Verhoef, W., Guo, Y., van der Tol, C., Li, Y., Huang, Y., 2016. FluorWPS: A Monte Carlo ray-tracing model to compute sun-induced chlorophyll fluorescence of three-dimensional canopy. Remote Sens. Environ. 187, 385–399.